Tailoring Electron-Transfer Barriers for Zinc Oxide/C_{60} Fullerene Interfaces

Philip Schulz, Leah L. Kelly, Paul Winget, Hong Li, Hyungchul Kim, Paul F. Ndione, Ajaya K. Sigdel, Joseph J. Berry, Samuel Graham, Jean-Luc Brédas, Antoine Kahn, and Oliver L. A. Monti**

The interfacial electronic structure between oxide thin films and organic semiconductors remains a key parameter for optimum functionality and performance of next-generation organic/hybrid electronics. By tailoring defect concentrations in transparent conductive ZnO films, we demonstrate the importance of controlling the electron transfer barrier at the interface with organic acceptor molecules such as C_{60}. A combination of electron spectroscopy, density functional theory computations, and device characterization is used to determine band alignment and electron injection barriers. Extensive experimental and first principles calculations reveal the controllable formation of hybridized interface states and charge transfer between shallow donor defects in the oxide layer and the molecular adsorbate. Importantly, it is shown that removal of shallow donor intragap states causes a larger barrier for electron injection. Thus, hybrid interface states constitute an important gateway for nearly barrier-free charge carrier injection. These findings open new avenues to understand and tailor interfaces between organic semiconductors and transparent oxides, of critical importance for novel optoelectronic devices and applications in energy-conversion and sensor technologies.

1. Introduction

The physical and chemical phenomena at the interface between functional oxide surfaces and thin molecular films are of fundamental relevance for organic and hybrid organic/inorganic electronic applications. A new generation of thin-film organic solar cells relies on a rationally designed organic/inorganic interfacial electronic structure in order to facilitate efficient charge extraction. Establishing a first-principles understanding of and precise control over this critical region in organic and hybrid photovoltaic (PV) devices has the potential to afford light-weight, flexible, and inexpensive alternatives to the prevailing energy conversion technologies.[1] A significant hurdle towards the rational design of more efficient organic photovoltaics (OPV) lies in the efficient extraction of photogenerated charge carriers at the contact. Despite numerous attempts to tailor the electronic properties of this junction,[2] a clear chemical and physical picture that is able to describe charge-harvesting across this interface is still in its infancy.[3,4] Such an understanding is of paramount importance for the ability to tailor carrier extraction during operation and hence device functionality along with overall device performance.

Inverted architectures, where thin transparent transition metal oxide interlayers are utilized at the bottom of the cell stack[5,6] have emerged as particularly promising designs. These yield highest efficiencies and prolonged lifetime by avoiding reactive metal top cathodes, and partially mitigate the requirement for encapsulation.[7,8] Low work function, highly conductive oxides such as TiO_2 or ZnO have been tested with reasonable success.[9] Most recently, research efforts have primarily focused on thin films of ZnO due to its high natural abundance and inexpensive processing at low temperatures.[10,11] Depending on the processing technique, steps, and parameters, the resulting ZnO surface exhibits a high density of bulk and near-surface defects, which govern carrier density, chemical potential and the chemistry with the adjacent organic layers.[12]

It has been well documented that ZnO is host to many native bulk defects, which change the degree of doping and in turn result in a change of the Fermi level position in the gap

Dr. P. Schulz,[+] Prof. A. Kahn
Department of Electrical Engineering
Princeton University
Princeton, New Jersey 08544, USA
E-mail: phschulz@princeton.edu
L. L. Kelly,[+] Prof. O. L. A. Monti
Department of Chemistry and Biochemistry
University of Arizona
Tucson, Arizona 85721, USA
E-mail: monti@u.arizona.edu
Dr. P. Winget, Dr. H. Li, Prof. J.-L. Brédas
School of Chemistry and Biochemistry and
Center for Organic Photonics and Electronics
Georgia Institute of Technology
Atlanta, Georgia 30332–0400, USA
H. Kim, Prof. S. Graham
School of Mechanical Engineering and
Center for Organic Photonics and Electronics
Georgia Institute of Technology
Atlanta, Georgia 30332–0250
Dr. P. F. Ndione, Dr. A. K. Sigdel, Dr. J. J. Berry
National Center for Photovoltaics
National Renewable Energy Laboratory
Golden, Colorado 80401, USA
[+]These authors contributed equally to this work.

DOI: 10.1002/adfm.201401794

as well as its chemical reactivity.[12–16] Studies of the chemical reactivity of ZnO and its defects have been performed largely with small adsorbates such as e.g., H_2O and CO_2 on single crystal ZnO substrates. An understanding of the interaction of defects in conductive thin film ZnO, used in actual devices, with π-conjugated organic semiconductors is however still lacking.[13,15] Donor defects such as oxygen vacancies (O_V), zinc interstitials (Zn_i), and atomic hydrogen are likely to play a large role in the interfacial interactions with organic thin films,[14] with likely major repercussions for performance of organic electronic devices. This clearly raises questions of the chemical interactions between ZnO contacts or interlayers, defect sites in these layers, and the active organic layer. Rational control over and mitigation of the impact of defects in ZnO layers in particular and transparent oxides in general promises thus to be a key step towards an improved understanding of the critical factors determining interfacial electronic structure.

Here we investigate the interface between an electron harvesting electrode, ZnO, and a prototypical acceptor molecule, C_{60}. C_{60} closely mimics the most common high-performing acceptor molecules in organic and hybrid solar cells such as PCBM and ICBA.[17] Unlike other small molecule surface modifiers that typically contain reactive functional groups[18] and unlike linear and planar molecules,[16] the high molecular symmetry enables us to largely neglect the effect of orientation of the adsorbed species at the ZnO surface. Robust chemical stability and respectable electrical conductivity allow for a clear tracking of electronic alignment in spectroscopic techniques.[19]

We present a unique approach to dissect the chemical and physical interactions at the ZnO/C_{60} interface. We start with a high conductivity ZnO film used in high-efficiency organic solar cells (OSCs).[20,21] We are able to tailor defect density and composition at the surface, and we study the electronic consequences on the bare ZnO surface by direct and inverse photoemission spectroscopy (PES/IPES). Subsequently, C_{60} thin-films are evaporated from sub-monolayer coverage to thicknesses of 10 nm. PES/IPES is used to trace the alignment of the frontier molecular orbitals with respect to the valence and conduction bands of zinc oxide as a function of the tailored defect structure at the interface. In particular, the offset between the lowest unoccupied molecular orbital (LUMO) of C_{60} and the conduction band minimum (CBM) of zinc oxide defines the barrier for electron extraction. We use density functional theory methods to model the interfacial electronic properties of ZnO with various defect sites, finding excellent agreement with the proposed configuration from the PES experiments. Finally, we introduce simple device stacks consisting of ZnO/C_{60} films and measure current density – voltage characteristics (j-V). This final step allows us to understand and predict the impact of the interfacial electronic structure at the tailored ZnO surfaces and the respective potential barrier formation on the functionality of OPV devices. The reduction of the interfacial barrier for electrons enhances the extraction current and improves device ideality and performance.

2. Bare and Sputtered ZnO Surfaces

We first discuss the electronic properties of the bare ZnO surfaces and their response to Ar^+ sputtering, and show that we are able to tailor controllably defect densities and types in such high-conductivity transparent oxide films. As a primary indicator for the surface electronic properties, the work functions of three thin-film ZnO surfaces with different surface treatments (untreated, soft- and hard-sputtered, i.e., no sputtering, sputtering at a kinetic energy of 0.5 keV at 0.4 μA ion current on the sample and at a kinetic energy of 1 keV with 10 μA ion current on the sample, respectively) were determined from the secondary electron cut-off of the UPS spectra (**Figure 1**a, 1c), resulting in values of 3.7(1) eV, 4.0(1) eV, and 4.5(1) eV, respectively, as summarized in **Table 1**.

Thus, an increase in Ar^+ sputtering kinetic energy and current yields an increase in work function. The valence band onset was determined from the He I and He II UPS spectra (Figure 1b, 1d) to be 3.2(1) eV, 3.2(1) eV and 2.8(1) eV below the Fermi level (E_F), resulting in an ionization energy (IE) of 6.9(1) eV, 7.2(1) eV and 7.3(1) eV, respectively, for the three different ZnO surfaces. This means that while the low-energy sputter process increases the work function and ionization energy (IE) of the ZnO surface, the position of the valence band onset with respect to E_F is only affected by the high kinetic energy ion treatment, reflecting a change in the chemical potential by this process.

Figure 1e shows the IPES spectrum of each surface, including the extrapolated conduction band minimum. The conduction band onset of each surface is found at 0.3(1) eV, 0.3(1) eV, and 0.5(1) eV above E_F, increasing somewhat with the extent of treatment. Here too, the hard-sputtered surface exhibits a pronounced shift of the band onset. The respective electron affinities (EAs) calculated from these values in conjunction with the work functions are 3.4(1) eV, 3.7(1) eV, and 4.0(1) eV. These results are summarized in **Table 2**.

The observed changes in work function, IE and EA go hand-in-hand with the appearance of tail states extending into the bandgap: we observe a valence band tail that reaches deep into the bandgap with increased sputtering energy. Changes in tailing of both valence and conduction bands can be associated with different concentrations and different types of defects in the near-surface region.[16] The strong tailing visible from the valence band suggests the presence of a significant density of deep lying defects in the 1 keV Ar^+ sample, with likely consequences for the work function change as well. At the same time, the untreated and soft-sputtered surfaces present a conduction band minimum lying close to E_F. This suggests the presence of a significant concentration of shallow donor defects in the near surface region probed by our experiments. Given the fact that the band gap derived from UPS /IPES measurements amounts to 3.5 eV and is only decreased marginally to 3.3 eV in case of the hard-sputtered film, the shift of the Fermi level must originate from a change in effective dopant concentration. In this picture, the surface sputtered with high kinetic energy ions introduces mild band bending in the near-surface region (0.3 eV) due to removal of shallow donors. By sputtering with high kinetic energy ions, a less *n*-type ZnO surface is produced with larger VB tailing, indicating a change in defect type and density at the surface. In order to understand these large differences more clearly, DFT calculations were performed.

Due to the mixture of surfaces present (see SI), we modeled the non-polar (100) surface. The calculated work function

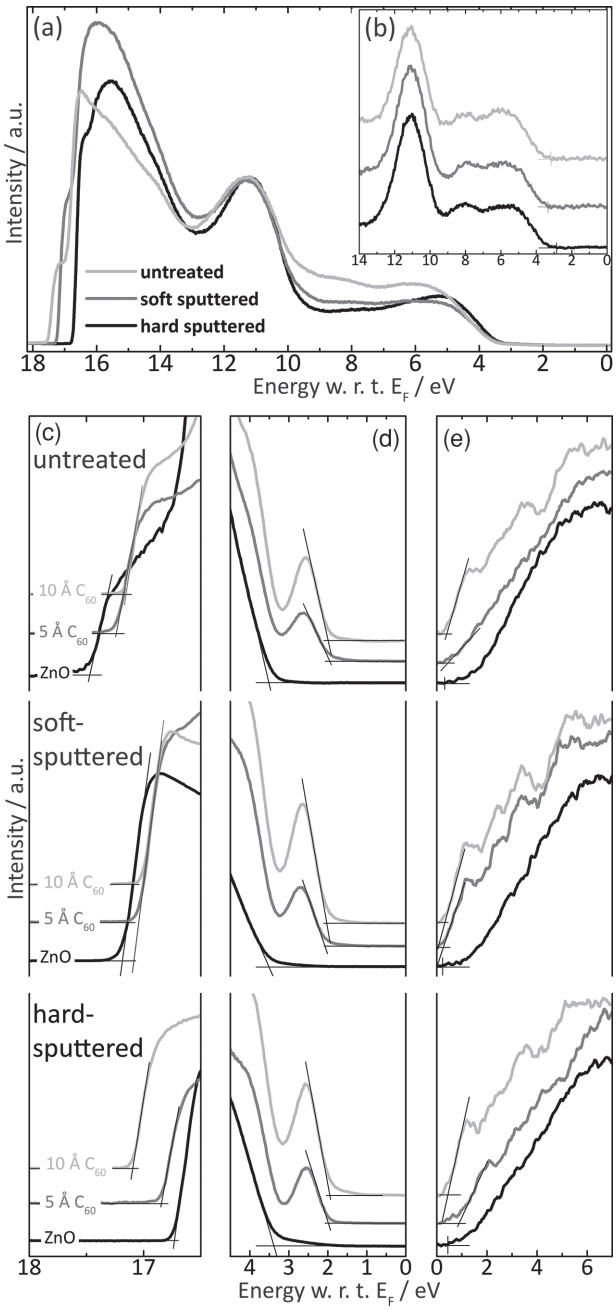

Figure 1. UPS/IPES spectra of ZnO surfaces with incremental coverage of C_{60} layers. UPS He I spectra (a) and He II spectra (b) spectra yield the work function and valence band region of the plain surfaces. Changes in work function upon adsorption of up to one monolayer of C_{60} is seen from the secondary electron cut-off in the He I spectra (c). The valence band region including the C_{60} HOMO level is tracked in the He I spectra (d). IPES measurements (e) show the conduction band of the ZnO surfaces and its evolution with adsorption of C_{60} layers.

for the stoichiometric (100) surface is shown in Table 1. This value is qualitatively different from the experimentally observed work functions. We attribute this difference to the lack of adequately capturing the high conductivity of the ZnO films investigated here: high carrier concentrations are achieved by significant *n*-doping, e.g., by introducing different types of

Table 1. Work function, Φ, for bare ZnO surfaces.

ZnO surface	Work function Φ [eV]
Untreated[a)]	3.7
Soft-sputtered[a)]	4.0
Hard-sputtered[a)]	4.5
(100) Stoichiometric[b)]	4.58
(100) Zinc interstitials (Zn_i)[b)]	3.56
(100) Oxygen vacancies (O_v)[b)]	4.52
(002) Zinc vacancies (Zn_v)[b)]	3.41

[a)]measured for the three prepared surfaces; [b)]calculated for the (100) and Zn-(002) ZnO surfaces.

defects (such as oxygen vacancies O_V or zinc interstitials Zn_i) or by atomic hydrogen inclusion and hydroxide formation at the surface.[12,16,22,23]

We investigated the effect of including in our models representative intrinsic defects suggested to *n*-dope ZnO, i.e., O_V or Zn_i, and the resulting calculated work functions are also shown in Table 1. Including deep donor defects such as O_V in the (100) surface model yields a high work function of 4.52 eV. This agrees well with the experimentally determined work function for the hard-sputtered ZnO film. The hard-sputtered sample also has increased VB tailing. XPS measurements (see SI) reveal that the Zn/O ratio is increased, which indicates a predominant removal of oxygen species from the surface. This invasive procedure leaves a chemically altered surface dominated by deep donor defect sites such as O_V.[15] The inclusion of shallow donor defects, e.g., Zn_i, lowers the work function to 3.56 eV, a necessary step to reach the low work functions observed experimentally for untreated and soft-sputtered surfaces. Although semi-local exchange functionals can lead to erroneous descriptions of defect levels, PBE+U has been shown to yield an adequate representation in the case of ZnO.[24–26] Low work function polar (002) ZnO surfaces are obtained by the inclusion of Zn_V (at a surface density of $6.8 \times 10^{13}/cm^2$) and in particular OH groups (at a surface density of $3.8 \times 10^{14}/cm^2$), bringing the work function to 3.41 eV.[16]

We will show below that the latter surface model is however unable to explain our observations of the electronic structure at C_{60}/ZnO interfaces. Moreover, since XPS reveals a slight excess of zinc over oxygen atoms in the soft-sputtered films, a significant contribution of Zn_V can be excluded already at this stage. The good qualitative agreement between experimental and computational data allows us to attribute the origin of the low work

Table 2. Band offsets, electron affinity (EA) and work function (WF) of bare ZnO surfaces.[a)]

ZnO surface	CBM [eV]	VBM [eV]	EA [eV]	WF [eV]
Untreated[a)]	0.3	3.2	3.4	3.7
Soft-sputtered[a)]	0.3	3.2	3.7	4.0
Hard-sputtered[a)]	0.5	2.8	4.0	4.5

[a)]measured for the three prepared surfaces.

functions of the soft-sputtered and untreated ZnO surface to a substantial population of shallow donor defects, while the hard-sputtered ZnO surface is dominated by deep donor defects. We find the results on the work function change to be consistent with the observation of a Fermi level shift in the gap for the different sputter treatments. From XPS we find further that the soft-sputter treatment effectively cleans the surface from surfactants and leads to a mildly increased work function, while the defect composition is not changed significantly. Hence the electronic bands remain at fixed energy with respect to E_F. In contrast, hard-sputtering introduces in addition deep lying defects such as O_V, shifting work function, electron affinity and E_F. This combined experimental and theoretical study provides thus an atomistic model of the surface composition and electronic properties of thin conductive ZnO films. ZnO work function and valence and conduction band positions can all be tailored effectively by Ar^+ sputtering. Values from calculated ZnO surfaces, where the inclusion of shallow or deep donor defects (Zn_i or O_V) tailor the work function and other electronic properties of the ZnO, agree well with the experimental observations. The ability to tailor the defect density and character of highly conductive ZnO surfaces offers an opportunity to investigate the importance of these tail states in determining the interfacial electronic structure and energy level alignment at interfaces between this oxide and organic semiconductors.

3. C_{60} on ZnO

The tailored ZnO surfaces provide different surface electronic properties in terms of VBM and CBM positions as well as work function. We show next that these differences have immediate consequences for the interactions with a molecular acceptor layer and the corresponding interfacial electronic structure, leading to interfacial charge redistribution. This fact can be used to tailor the hybrid organic/inorganic interface. The presence and absence of charge transfer can be understood from the specific variations in the defect composition on the different ZnO surfaces, as shown both by our computational and spectroscopic results.

In Figures 1c-e we show the development of the interfacial electronic structure and band alignment for the different ZnO films and for C_{60} thicknesses up to 10 Å, as observed by UPS/IPES. Band offsets and vacuum level changes for the partial and complete monolayer as well as thicker layers obtained from these and similar spectra are summarized in **Figure 2**.

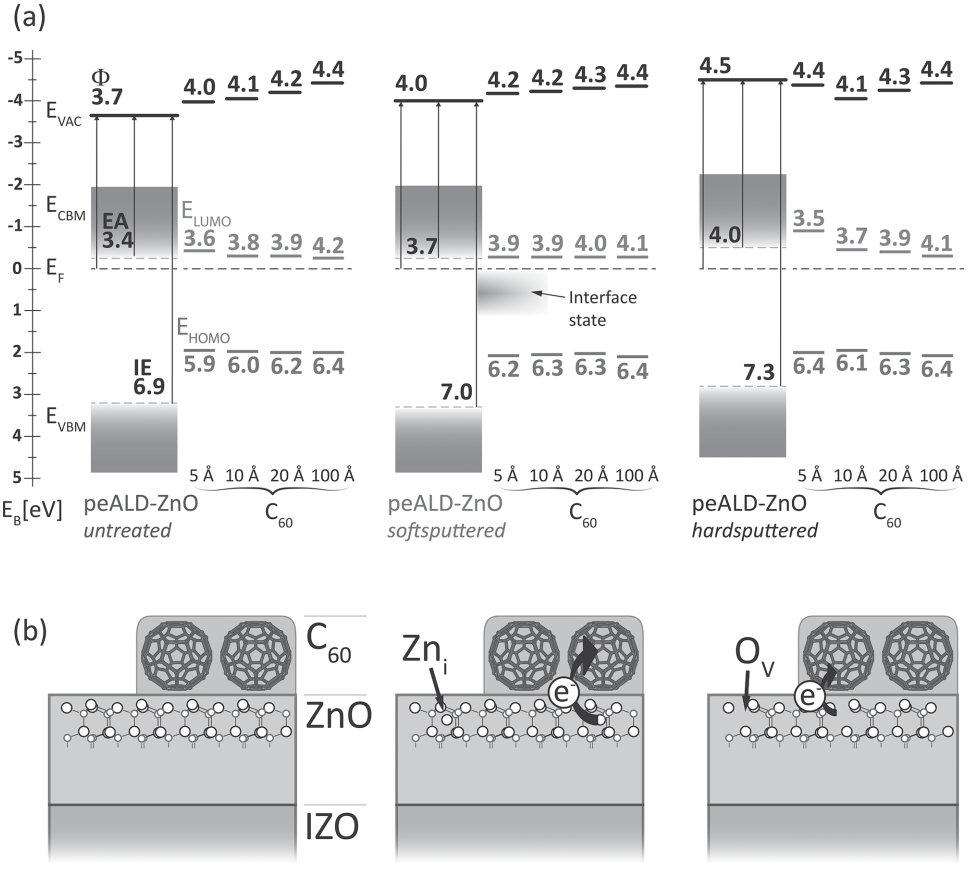

Figure 2. Energy diagram from the UPS/IPES measurements. a) The soft-sputtered ZnO shows only a small raise in work function which increases with additional layers of C_{60} with the shallow donor sites aligning with the LUMO. On hard-sputtered ZnO the first ML of C_{60} induces a decrease of the work function and barrier formation for electron-transfer between conduction band of the ZnO and LUMO of C_{60}. Proposed charge transfer mechanism b) for adsorbed C_{60} molecules on ZnO (b) with strong charge transfer to shallow donors (i.e., zinc interstials, Zn_i) and rather weak charge transfer to deep defects (i.e., oxygen vacancies, O_v).

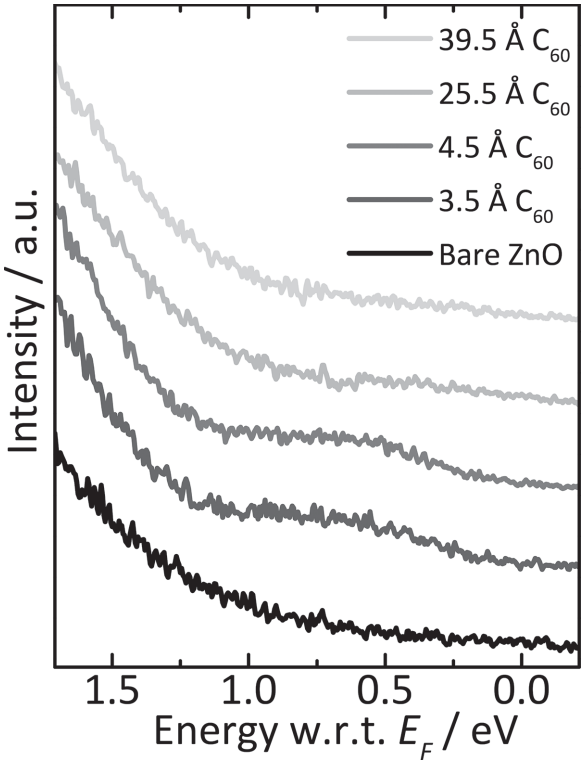

Figure 3. UPS spectra magnification of the near-Fermi region for C_{60} deposited on soft-sputtered ZnO. At low coverage, a weak spectroscopic feature is present with an onset slightly below E_F and peak center 0.6 eV from E_F, originating from a hybrid interface state between ZnO and C_{60}.

Though starting from different initial values, after adsorption of 10 Å of C_{60}, the experimental work functions are all rather similar, i.e., 4.1(1) eV (untreated), 4.2(1) eV (soft-sputtered) and 4.1(1) eV (hard-sputtered). This indicates that the interfacial electronic structure evolves differently for the three ZnO surfaces: The untreated and soft-sputtered sample displays a work function increase of 0.4 and 0.2 eV, respectively, whereas the hard-sputtered samples exhibits a work function decrease of –0.4 eV. A work function increase at an interface with a relatively unreactive, non-polar molecule such as C_{60} is strongly suggestive of charge transfer from ZnO to C_{60}.[27] Indeed, at C_{60} film thicknesses less than 20Å, a small feature appears in the valence band tail region between the HOMO and E_F (0.6 eV binding-energy peak center and onset slightly below E_F) in the case of soft-sputtered ZnO surface (**Figure 3**), and disappears at higher coverage. This feature arises therefore from an interfacial interaction, and its energy is indicative of a hybrid interface state with charge transfer character from ZnO to C_{60}. This is fully consistent with our assignment of the work function increase to charge-transfer across the interface.

These conclusions are indeed borne out also by the computational results, which show a work function increase and significant charge transfer for C_{60} adsorbed on ZnO in the presence of Zn_i defects (**Table 3**). An overlap between the C_{60} LUMO and a state with significant Zn_i character is observed in the calculated density of states (**Figure 4**(b)), resulting in a hybrid state around

Table 3. Change in work-function, $\Delta\Phi$, and its decomposition for the (100) and Zn-(002) surfaces upon C_{60} monolayer adsorption.

	$\Delta\Phi$/eV	ΔV_{SAM}/eV	$\Delta V_{int.\ dip.}$/eV	$\Delta V_{reorg.}$/eV	$q^{a)}$/e
(100) Stoic.	–0.23	0.00	–0.26	+0.03	–0.00
(100) Zn_i	–0.19	0.00	–0.21	+0.02	–0.01
(100) O_v	+0.83	0.00	+0.88	–0.04	–0.24
(002) Zn_V	+0.43	0.00	0.10	0.36	–0.01

[a)]charge q on C_{60} molecule. For other symbols, see eqn (1) in the Experimental Section.

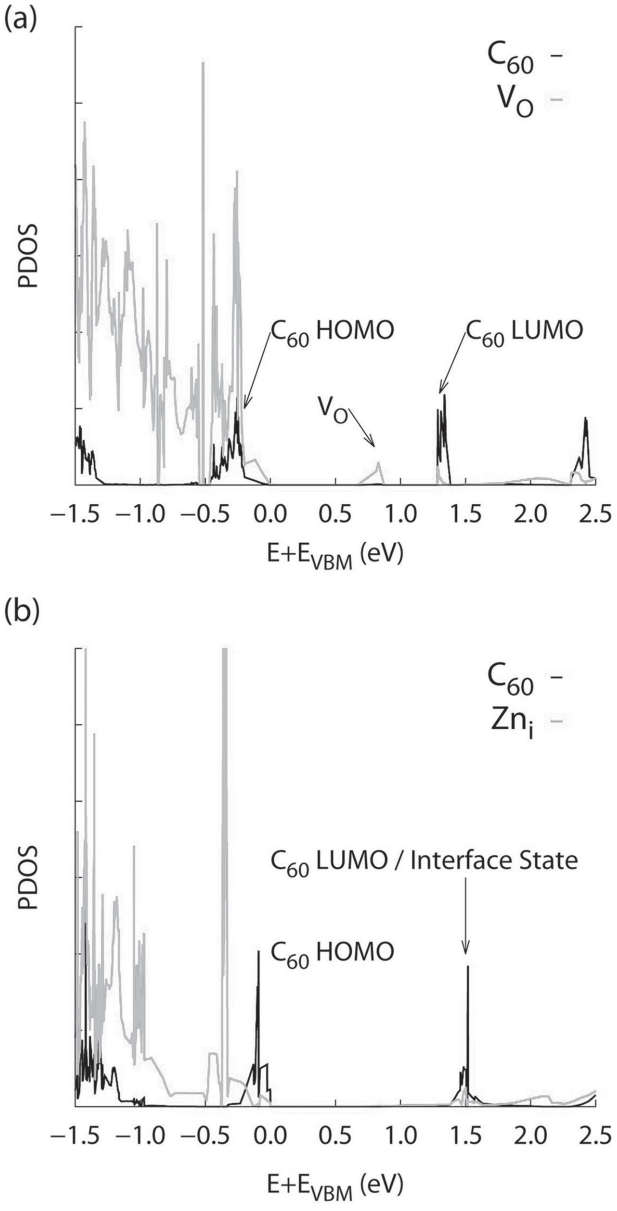

Figure 4. The density of states projected onto the surface and C_{60} (PDOS) for O_V and Zn_i rich ZnO surfaces. The valence band maximum is set equal to zero to provide unambiguous common reference energy for both surfaces.

E_F as observed experimentally (Figure 3). This suggests further that beyond charge transfer to C_{60}, hybridization is responsible for the precise energy of the experimental interface state. Indeed, this hybridization leads to a modest charge transfer at the C_{60}-ZnO interface (Table 3). These results also agree with charge-transfer observed at the ZnO/perylene diimide (PDI) interface.[14]

On the other hand, the work function decreases for the hard sputtered surface, and no interface states near E_F are observed. This is in excellent agreement with calculations for the ZnO surface dominated by O_V. The adsorption of C_{60} brings a work function decrease of about –0.2 eV, and the C_{60} LUMO is aligned with the CBM of ZnO in the calculated DOS (Figure 4). We note further that while hydroxylation and inclusion of Zn_V results in an increase of the work function as observed experimentally, no interface state and only incorrect band alignment is obtained (see Table 3 and projected density of states, PDOS, in SI).

Overall, shallow (strong) donors lead to a moderate electron transfer (0.24 e^-) to the fullerene, while the deep (weak) donor levels (O_V) yield no such transfer. Note that for stoichiometric surfaces, there is only a minor rearrangement of charge near the interface and no significant charge transfer to C_{60} either. We conclude that tailoring the electronic structure of ZnO surfaces has immediate consequences on the extent to which electronic states of acceptor molecules such as C_{60} are able to couple to the ZnO surface, both by interfacial hybridization and changes to the chemical potential. This underlines that characterizing the precise nature and density of defects in the near-surface region is critically important for developing a fundamental understanding of the factors that determine energy level alignment at such hybrid interfaces.

The differences noted above for interfaces formed on ZnO surfaces treated differently are also reflected in the experimentally observed LUMO and conduction band region. In Figure 1e the C_{60} LUMO onset is shown for each surface as a function of increasing coverage. In the case of the untreated and soft-sputtered surfaces, the C_{60} LUMO is initially pinned to E_F, and continues to be pinned at one monolayer coverage and above (Figure 2a). Pinning E_F to the LUMO level is in good agreement with charge transfer across this interface and consistent with the fact that interface states above the C_{60} HOMO observed in the UPS spectra are being filled by charge transfer from ZnO. The initial sub-monolayer coverage (5 Å) on the hard-sputtered sample yields very different energetics: The C_{60} LUMO is found 0.9 eV above E_F, and at 10 Å thickness shifts towards E_F, pinned only at higher coverages. The alignment of the LUMO with respect to the CBM is qualitatively reproduced in the calculated PDOS (Figure 4(a)).

Changes in work function, IE, and EA for thicknesses larger than 10 Å on the three surfaces are also shown in Figure 2a. As the thickness of C_{60} increases, all three surfaces converge towards the same electronic structure, representing as expected the properties of a bulk C_{60} film. At 100 Å the work function and HOMO/LUMO positions for each surface are the same. This demonstrates clearly the interfacial nature of the interactions observed at the different ZnO/C_{60} interfaces.

In summary, we have identified charge transfer between different defect sites on ZnO surfaces and C_{60} molecules as a critical mechanism determining energy level alignment at this interface. Calculations indicate that the shallow donor sites undergo hybridization with the fullerene, leading to charge transfer and a good alignment of the LUMO with the conduction band minimum of ZnO. Deep donors exhibit almost no charge transfer and presumably result in the formation of a barrier for electron transfer from the molecular film to the oxide layer. We next use electrical (j-V) characterization to show how such a defect-driven barrier formation influences charge injection/extraction processes through this interface.

4. Electronic Transport across the C_{60}/ZnO Interface

The electronic energy level alignment at the various C_{60}/ZnO interfaces has clear implications for charge injection and extraction between the two materials. We investigate this impact of the different interfacial energy landscapes by measuring transport properties in device architectures made from a 50 nm thin film of C_{60} sandwiched between a mercury electrode and the different ZnO surfaces. C_{60} has a far lower intrinsic mobility for holes than for electrons,[28] and for all three surfaces the VBM is deep and far below the C_{60} HOMO, resulting in a potential barrier of at least 1 eV for hole extraction from C_{60} into the ZnO layer. Hole transport in such devices can thus be neglected.

Vertically probed j-V characteristics of such electron-only devices including the different ZnO surfaces demonstrate the importance of a barrier-free contact for electron transport (**Figure 5**). Curves for the untreated and the soft-sputtered ZnO samples are nearly symmetric in forward and reverse bias, indicating the absence of a significant contact barrier with electron injection equally efficient in both directions. Such a behavior is expected from the electron spectroscopy results, where the Fermi level was found pinned to the LUMO of C_{60} right at the interface. Moreover, transport is further facilitated by hybrid interface states formed between C_{60} and shallow donor states, which chemically couples the molecule to the surface.

In contrast, the j-V curve for the hard-sputtered ZnO surface exhibits clear asymmetry. The current is lower in forward than in reverse bias, indicating the presence of an injection barrier for electrons from ZnO into C_{60}. This finding is in excellent agreement with the spectroscopic results in Figure 2a, revealing an injection barrier of 0.4 eV.

In order to fully understand the electrical behavior, a separation of the j-V characteristics into three regions is useful: region I accounts for forward bias with the positive potential on the mercury, region II spans over the low (<1V) reverse bias regime, and region III is defined for higher values of the reverse bias. In this way, we account for a contact barrier that is spatially confined to the first monolayer, as a result of the changing LUMO position in the C_{60} film as a function of thickness. The entirety of the forward bias characteristics (i.e., region I) is described with a constant barrier. For the hard-sputtered ZnO surface, the curve shows the same diode behavior as devices incorporating untreated and soft-sputtered surfaces, but with current densities lower by almost two orders of magnitude. In reverse bias, the barrier is of equal importance for low voltages (II), but

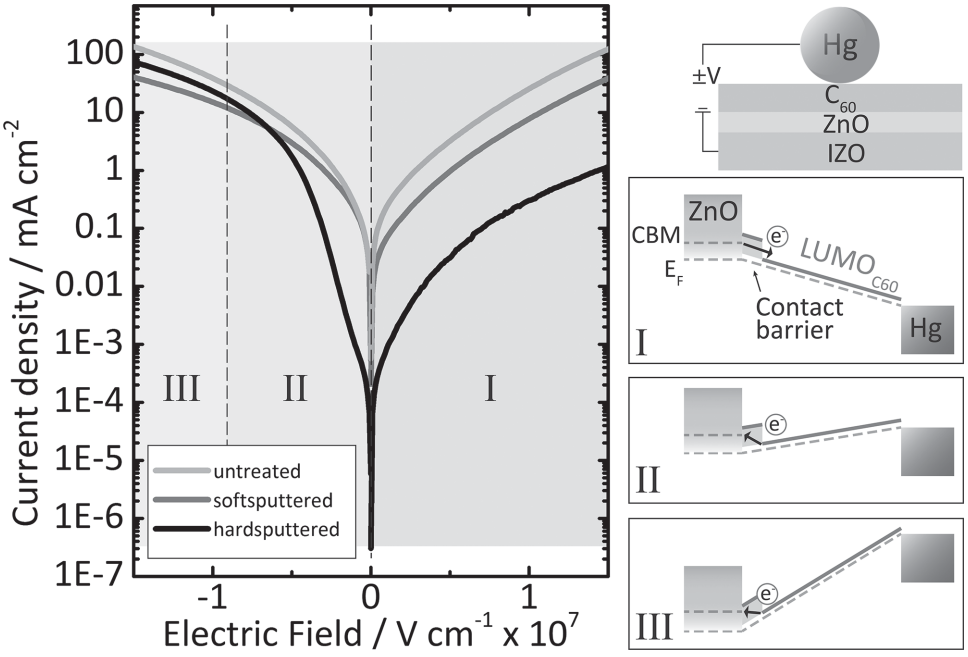

Figure 5. j-V curves from mercury probe measurements of C_{60} on top of the various ZnO surfaces. Untreated and soft-sputtered ZnO contacts give symmetric diode characteristics. The electron transfer barrier present for the case of the hard-sputtered ZnO surface leads to different device behavior in three distinguishable transport regimes: Reduced current due to poor electron injection in forward bias (I), reduced current and double diode characteristic at low reverse bias due to poor electron extraction (II) and eventually regular diode behavior at large extraction voltages (III).

between 0 V and 0.5 V the curve switches to a behavior characteristic of a field-dependent transfer barrier. Indeed raising the potential on the side of the mercury droplet leads to a stronger extraction field and allows for more facile transport through the barrier, a behavior that persists to a bias around 1 V. At larger voltages, all three films behave identically (III).

In summary, the progression of the j-V curves demonstrates directly the impact of the formation of a barrier for electron transfer between C_{60} and ZnO that stems from a substantial concentration of deep donor defects, as uncovered by our combined spectroscopic and computational approach. Moreover, our results demonstrate how a barrier-free ZnO surface leads to efficient charge collection from the active layer. These results also provide a precise picture of the potential benefits that the presence of shallow donor defects brings to ZnO, permitting greater flexibility in serving as an interlayer material for electrodes in organic electronics. Beyond enhancing the ZnO thin film electronic structure, the interaction between defect sites and acceptor molecule presents an effective avenue to facilitate efficient carrier extraction and to prevent the formation of a substantial interfacial barrier. These findings suggest a novel way of tailoring complex hybrid organic/oxide interfaces for next-generation energy conversion platforms and hybrid optoelectronics.

5. Conclusion

In this study, we have shown that the interfacial electronic properties of a prototypical transparent conducting electrode material can be tailored, with direct consequences for the electronic structure of hybrid organic/inorganic interfaces. Using Ar^+ sputtering, we are able to modify the type and concentration of specific ZnO surface defects (deep and shallow donors). A change in defect concentrations and type substantially alters the interface energy level alignment with, and coupling to, acceptor molecules such as C_{60}. The resulting differences in energy level alignment are shown to be important for charge injection/extraction from/to ZnO, where high concentrations of deep donors produce a barrier for charge injection from C_{60} into ZnO while shallow donor sites enable facile electron transfer. These results are likely general and point the way towards a rational design for efficient carrier extraction at hybrid organic/inorganic electrode interfaces.

6. Experimental Section

ZnO Preparation: As a highly planar substrate for ZnO film growth, conductive (σ >2000 S/cm) indium zinc oxide (IZO) films were prepared by sputter deposition on glass substrates, cleaned with acetone and isopropanol prior to thin film fabrication. Subsequently, ZnO was grown on the planarized IZO substrate by plasma-enhanced atomic layer deposition (peALD). peALD was carried out at 100 °C and 0.4 Torr using a Fiji system (Cambridge Nano Tech). As a precursor, diethyl zinc was pulsed into an argon carrier gas line and delivered into the processing chamber, followed by purging the chamber for 60 sec to remove residual precursor. After that, a remote oxygen plasma was created using 30 sccm oxygen at 300 W RF power, supplied to the chamber for 20 sec as an oxidizer. Subsequently, the chamber was purged for 10 sec. For the ZnO film fabrication, 200 cycles were repeated which yielded a ZnO film thickness of approximately 20 nm, measured using spectroscopic ellipsometry on a Si witness sample grown simultaneously during the process (M-2000, J. A. Woollam Co.). The peALD-ZnO films grown in this fashion were found to be polycrystalline, oriented towards both

(100) and (002) faces as found in X-ray diffraction experiments (see Supporting Information, SI).

ZnO Surface Modification: ZnO films were Ar^+-sputtered under various conditions in order to introduce defects in a controlled fashion. For *soft sputtering,* ion energies of 500 eV and sample currents of 0.4 μA were used, while for *hard sputtering* ion energies of 1 keV and currents of 10 μA were used. In each case, the substrate was sputtered for 45 min. After either treatment, the adventitious carbon levels were below the detection threshold of XPS.

C_{60} Film Deposition: C_{60} layers were evaporated on top of the in situ treated ZnO surfaces from a Knudsen cell evaporator at a rate of 2 Å min^{-1}, monitored on a quartz crystal microbalance. Note that a thickness of 10 Å roughly corresponds to a coverage of one monolayer of C_{60}. Subsequently, the samples were transferred in situ to the analysis chamber for recording direct and inverse photoemission spectra. For device studies of the current density versus voltage response (j-V measurements), C_{60} layers were grown at a rate of 0.5 Å s^{-1} and transferred under controlled atmosphere to a Hg-probe station placed in a N_2 glove box.

Measurements and Characterization: Ultraviolet and X-ray photoemission spectroscopies (UPS/XPS) were performed in a custom built ultra-high vacuum system at Princeton University and in a Kratos Axis Ultra spectrometer at the University of Arizona. He I (21.22 eV) and He II (40.8 eV) excitation lines from a helium plasma discharge lamp were employed for the UPS measurements, while Al Kα radiation (1486.7 eV) was used for XPS spectra. Inverse photoemission experiments (IPES) were performed in isochromat mode, using a set-up described elsewhere.[29] The instrumental resolution was 150 meV, 850 meV and 400 meV for UPS, XPS and IPES, respectively. j–V curves were acquired in double sweep mode with a BASi Controlled Growth Mercury Electrode setup, averaging over 20 scans for each sample.

Electronic-Structure Calculations: DFT electronic-structure calculations were performed using the Vienna Ab initio Package (VASP).[30] A generalized-gradient approximation (GGA) exchange-correlation functional of Perdew, Burke, and Ernzerhof (PBE)[31,32] was used with the projector-augmented wave (PAW) method (energy cut-off set at 400 eV).[33] The GGA+U approximation[31] with an effective Hubbard U-parameter (U_{eff} = 8.5 eV)[35] was implemented to describe the strongly localized zinc 3d-orbitals. Earlier work indicates that this parameter results in a calculated band gap of 1.8 eV,[16] smaller than the experimental value of 3.3–3.4 eV.[36] The band gap calculated for C_{60} adsorbed on the ZnO surface is however underestimated in a similar fashion. While error-cancelation is nontrivial, the relative band-offsets for these materials are well reproduced. Therefore, the relevant physics are retained at this interface. We use a DFT-D approach to include van der Waals interactions, adding an empirical potential to the DFT energy.[37] Optimization of geometries utilized only the high-symmetry Γ-point; geometries were considered converged when the maximal residual force on each atom was less than 0.05 eV/Å. Energy properties were then calculated using a $2 \times 2 \times 1$ grid of k-points. The atomic charges were estimated within the Bader scheme.[38,39] The ZnO thin films exhibit several different crystal faces. We examined therefore both the nonpolar (100) and the polar zinc-terminated (002) surfaces of ZnO in the calculations. For the (100) surface, an orthogonal unit cell was modeled using ten Zn-O layers with dimensions of 13.00 Å × 10.41 Å in the (110) and (001) directions and 36.00 Å in the (100) direction. The zinc-terminated ZnO (002) surface was considered with a surface unit cell with dimensions of 13.00 × 11.26 Å, containing one zinc vacancy (V_{Zn}) and six OH groups to ensure surface electron charge neutrality. As prepared samples of ZnO films are inherently n-doped, a low concentration of either oxygen vacancies (O_v, one per 80 oxygen atoms) or zinc interstitials (Zn_i, one per 80 zinc atoms) was introduced in the near-surface region. The defects included here capture the essential characteristics of n-ZnO even though other mechanisms for unintentional *n*-type doping have been discussed,[12] by providing both prototypical deep (O_v) and shallow (Zn_i) donors previously observed on or near the surface.[25,40–42] For each surface, C_{60} adsorption sites were found by moving the fullerene across the surface unit cell, with further geometry optimizations carried out for the lowest energy sites. We also assessed the importance of different orientations of the fullerene with respect to the surface, i.e., with the 5-membered and 6-membered rings parallel to the surface. In the calculations reported here, we use only the lowest-energy structures. We anticipate that the non-specific nature of the defect/C_{60} interaction is dominated by the Fermi-level of the films, and that Schottky, Frenkel and other multicenter defects are characterized by the energies of their defect level; thus periodic DFT calculations capture the essential physics of the composition-dependent and tailored interfacial charge-transfer at the C_{60}/ZnO interface. In order to fully understand the origin of the observed differences in work function and charge transfer, we partitioned the change in work-function into three contributing components:[18]

$$\Delta\Phi_{calc} \approx \Delta V_{SAM} + \Delta V_{int.dip.} + \Delta V_{geom.reorg.} \quad (1)$$

where ΔV_{SAM} is the potential energy difference of an electron crossing the C_{60} monolayer suspended in vacuum at the same geometry as when adsorbed on the ZnO surface; $\Delta V_{int.dip.}$, the potential energy difference of an electron due to the charge redistribution occurring directly at the interface between the monolayer and the ZnO slab (interfacial dipole); and $\Delta V_{geom.reorg.}$, the change in potential energy due to geometry reorganization of the ZnO surface upon adsorption of the C_{60} monolayer.

Supporting Information

Supporting Information is available from the Wiley Online Library or from the author. Supporting Information contains X-ray Diffraction and X-ray photoemission data of ZnO films and further computational details.

Acknowledgements

This work was supported as part of the Center for Interface Science: Solar Electric Materials (CISSEM), an Energy Frontier Research Center funded by the U.S. Department of Energy, Office of Science, Basic Energy Sciences under Award Number DE-SC0001084. The computations at Georgia Tech reported here were performed mainly at the Georgia Tech Center for Computational Molecular Science and Technology, funded through a NSF CRIF award (Grant CHE-0946869) and by the Georgia Institute of Technology.

Received: June 2, 2014
Revised: August 19, 2014
Published online: October 1, 2014

[1] J. A. Carr, S. Chaudhary, *Energy Environ. Sci.* **2013**, *6*, 3414.
[2] S. K. Hau, H.-L. Yip, N. S. Baek, J. Zou, K. O'Malley, A. K. Y. Jen, *Appl. Phys. Lett.* **2008**, *92*, 253301.
[3] Y. Xu, O. T. Hofmann, R. Schlesinger, S. Winkler, J. Frisch, J. Niederhausen, A. Vollmer, S. Blumstengel, F. Henneberger, N. Koch, P. Rinke, M. Scheffler, *Phys. Rev. Lett.* **2013**, *111*, 22802.
[4] R. Schlesinger, Y. Xu, O. T. Hofmann, S. Winkler, J. Frisch, J. Niederhausen, A. Vollmer, S. Blumstengel, F. Henneberger, P. Rinke, M. Scheffler, N. Koch, *Phys. Rev. B* **2013**, *87*, 155311.
[5] M. T. Lloyd, C. H. Peters, A. Garcia, I. V. Kauvar, J. J. Berry, M. O. Reese, M. D. McGehee, D. S. Ginley, D. C. Olson, *Sol. Energy Mater. Sol. Cells* **2011**, *95*, 1382.
[6] A. K. K. Kyaw, D. H. Wang, V. Gupta, J. Zhang, S. Chand, G. C. Bazan, A. J. Heeger, *Adv. Mater.* **2013**, *25*, 2397.
[7] O. Pachoumi, C. Li, Y. Vaynzof, K. K. Banger, H. Sirringhaus, *Adv. Energy Mater.* **2013**.
[8] Z. He, C. Zhong, S. Su, M. Xu, H. Wu, Y. Cao, *Nature Photonics* **2012**, *6*, 591.

[9] H. Oh, J. Krantz, I. Litzov, T. Stubhan, L. Pinna, C. J. Brabec, *Sol. Energy Mater. Sol. Cells* **2011**, *95*, 2194.
[10] W. J. E. Beek, L. H. Slooff, M. M. Wienk, J. M. Kroon, R. A. J. Janssen, *Adv. Funct. Mater.* **2005**, *15*, 170.
[11] Y. Sun, J. H. Seo, C. J. Takacs, J. Seifter, A. J. Heeger, *Adv. Mater.* **2011**, *23*, 1679.
[12] D. C. Look, G.C Farlow, P. Reunchan, S. Limpijumnong, S. B. Zhang, K. Nordlund, *Phys. Rev. Lett.* **2005**, *95*, 225502
[13] R. Lindsay, E. Michelangeli, B. G. Daniels, T. V. Ashworth, A. J. Limb, G. Thornton, A. Gutiérrez-Sosa, A. R. Baraldi, S. Lizzit, *J. Am. Chem. Soc.*, **2002**, *124*, 7117.
[14] P. Winget, L. K. Schirra, D. Cornil, H. Li, V. Coropceanu, P. F. Ndione, A. K. Sigdel, D. S. Ginley, J. J. Berry, J. Shim, H. Kim, B. Kippelen, J.-L. Brédas, O. L. A. Monti, *Adv. Mater.* **2014**, *26*, 4711.
[15] C. Wöll, *Prog. Surf. Sci.* **2007**, *82*, 55.
[16] H. Li, L. K. Schirra, J. Shim, H. Cheun, B. Kippelen, O. L. A. Monti, J.-L. Brédas, *Chem. Mater.* **2012**, *24*, 3044.
[17] C.-Z. Li, H.-L. Yip, A. K. -Y. Jen, *J. Mater. Chem.* **2012**, *22*, 4161.
[18] H. Li, P. Paramonov, J.-L. Brédas, *J. Mater. Chem.* **2010**, *20*, 2630.
[19] M. L. Tietze, M. Riede, K. Leo, K. Vandewal, S. Olthof, W. Tress, S. Pfützner, C. Schünemann, L. Burtone, P. Schulz, A. Kahn, *Phys. Rev. B* **2013**, *88*, 085119
[20] J.-C. Wang, W.-T. Weng, M.-Y. Tsai, M.-K. Lee, S.-F. Horng, T.-P. Perng, C.-C. Kei, C.-C. Yuc, H.-F. Meng, *J. Mater. Chem.* **2010**, *20*, 862.
[21] H. Cheun, C. Fuentes-Hernandez, Y. Zhou, W. J. Potscavage, Jr., S.-J. Kim, J. Shim, A. Dindar, B. Kippelen, *J. Phys. Chem. C* **2010**, *114* , 20713.
[22] A. K. Sigdel, P. F. Ndione, J. D. Perkins, T. Gennett, M. F. A. M. van Hest, S. E. Shaheen, D. S. Ginley, J. J. Berry, *J. Appl. Phys.* **2012**, *111*, 093718.
[23] E. R. Ratcliff, A. K. Sigdel, M. R. Macech, K. Nebesny, P. A. Lee, D. S. Ginley, N. R. Armstrong, J. J. Berry, *Thin Solid Films* **2012**, *520*, 5652.
[24] S. Lany, A. Zunger, *Phys. Rev. B* **2010**, *81*, 113201.
[25] A. Janotti, C. G. Van De Walle, *Phys. Rev. B*, **2007**, *76*, 165202.
[26] A. Boonchun, W. R. L. Lambrecht, *Phys. Stat. Sol.* **2011**, *248*, 1043.
[27] H. Ishii, K. Sugiyama, E. Ito, K. Seki, *Adv. Mater.* **1999**, *11*, 605.
[28] R. Könenkamp, G. Priebe, B. Pietzak, *Phys. Rev. B* **1999**, *60*, 11804.
[29] C. I. Wu, Y. Hirose, H. Sirringhaus, A. Kahn, *Chem. Phys. Lett.* **1997**, *272*, 43.
[30] a)G. Kresse, J. Furthmüller, *Comput. Mat. Sci.* **1996**, *6*, 15; b) G. Kresse, J. Furthmüller, *Phys. Rev. B* **1996**, *54*, 11169.
[31] J. P. Perdew, K. Burke, M. Ernzerhof, *Phys. Rev. Lett.* **1996**, *77*, 3865.
[32] J. P. Perdew, K. Burke, M. Ernzerhof, *Phys. Rev. Lett.* **1997**, *78*, 1396.
[33] P. E. Blöchl, *Phys. Rev. B* **1994**, *50*, 17953.
[34] S. L. Dudarev, G. A. Botton, S. Y. Savrasov, C. J. Humphreys, A. P. Sutton, *Phys. Rev. B* **1998**, *57*, 1505.
[35] P. Palacios, K. Sanchez, P. Wahnon, *Thin Solid Films* **2009**, *517*, 2448.V.
[36] V. Srikant, D. R. Clarke, *J. Appl. Phys.* **1998**, *83*, 5447.
[37] S. Grimme, *Chem. Phys. Lett.* **1996**, *259*, 128.
[38] R. F. W. Bader, A. Larouche, C. Gatti, M. T. Carroll, P. J. MacDougall, K. B. Wiberg, *J. Chem. Phys.* **1987**, *87*, 1142
[39] W. Tang, E. Sanville, G. Henkelman, *J. Phys.: Compute Mater* **2009**, *21*, 084204.
[40] W. Göpel, L. J. Brillson, C. F. Brucker, *J. Vac Sci. Technol.* **1980**, *17*, 894.
[41] H. Zheng, J. Kröger, R. Berndt, *Phys. Rev. Lett.* **2012**, *108*, 076801.
[42] H. Zheng, A. Weismann, R. Berndt, *Phys. Rev. Lett.* **2013**, *110*, 226101.